The role of surface stoichiometry in the activity of doped vanadia-based catalysts for the selective catalytic reduction

Mengru Li, Sung Sakong, Fabiola Dominguez-Flores, NaNa Ma, and Axel Groß[*]

Institute of Theoretical Chemistry, Ulm University, 89081 Ulm, Germany

E-mail: Axel.Gross@uni-ulm.de

Abstract

Mixing dopants into oxide catalysts can improve the catalytic activity, as shown in the dramatic boost of the NH_3 selective catalytic reduction (SCR) activity on vanadia catalysts upon doping by tungsten. Here, we employ first-principles calculations to study the influence of selected dopants (Ce, Zr, Nb, Mo, and W) in tungsta-vanadia on the SCR activity in terms of dopant concentration, distribution, and species. We demonstrate how the dopants affect the stoichiometry of the catalyst and thus fine-tune the local electron distribution and polarization in the catalytic layer. In addition, we address the relation between dopant concentration and the population of the active vanadyl configuration on the surface. Finally, we propose the generalized surface stoichiometry of the doped vanadia catalysts as a descriptor for the SCR catalytic activity, which promises to be instrumental in identifying oxide catalysts with improved properties also for other important catalytic reactions.

1

Introduction

A diverse structure and composition of metal oxides typically provides active sites for many redox reactions, such as selective and complete oxidation, dehydrogenation, or reductive coupling.[1-3] A basic understanding of the factors influencing the occurrence of these active sites can also be rather beneficial for the improvement of industrial processes, such as the reduction of nitrogen oxide (NO_x) emissions. The emission of nitrogen oxide from mobile and stationary sources still substantially contributes to air pollution. They are the cause of, among others, smog, acid, rain, ozone depletion and thus have an harmful impact on the global climate.[4,5] Consequently, there are strong ongoing efforts for converting nitrogen oxide emissions into less harmful products through suitable effective catalysts[6-11] Typical commercial metal oxide catalysts extensively applied in the industry usually consist of a catalytic layer on a support. The catalytic performance of the oxide layer can be further improved by mixing a certain portion of guest elements into the host oxide through doping, which leads to changes in the electronic structures and chemical bonds within the catalyst.[12]

One of the most widely employed dopants in commercial catalysts for the selective catalytic reduction (SCR) reaction to reduce nitrogen oxide emission is tungsten, as realized in WO_3-V_2O_5/TiO_2 (anatase).[13-16] The role of tungsten doping in improving the catalytic performance is still controversially discussed. Based on spectroscopy experiments, Peng et al. proposed that the increased concentration of Brønsted acid sites (V-OH) on catalyst layer by tungsten doping facilitates NH_3 adsorption.[17] On the other hand, more recent infrared spectroscopic studies[9,10] suggested that the terminal vanadyl groups, which act as Lewis acid sites, are crucial for stronger ammonia adsorption. Indeed, in a previous theoretical study,[8] we have shown that the addition of tungsten can lead to non-stoichiometric surfaces and the occurrence of unsaturated terminal vanadyl groups. Yet, both theory and experiment agree that a proper amount of tungsten stabilizes the anatase phase of the TiO_2 support thus extending the operation time of the catalyst with a high activity.[8,18] Still, although tungsta-vanadia catalysts exhibit an outstanding catalytic activity in the temperature win-

dow of 300-400°C, the low NO conversion rate at lower temperatures and the poor selectivity at high temperatures remain to be challenging issues. Therefore, numerous efforts have focused on the widening of the operation temperature range of SCR catalysts, which is closely related to adjusting the redox properties and the acidity of catalysts.[19–21]

Among various possibilities, introducing new doping elements is one of the most promising ways to optimize catalytic performance. Several experiments demonstrated that Ce,[22–24] Zr,[24] Mo,[25] and Nb[26–28] could be alternative dopants to tungsten. Ce doping broadens the operating temperature window and establishes better reducibility to produce Brønsted acid site for NH_3 adsorption. Zr doping increases the NO conversion rate to 80% at temperatures as low as 150°C.[24] Mo doping alters the type and abundance of acid sites.[25] Finally, Nb doping leads to a higher NO_x conversion rate at low temperature.[26,27] However, despite these successes, it is fair to say that dopant screening typically relies on trial and error attempts without necessarily invoking a clear strategy.

Due to the complexity of doped-oxide catalysts, the knowledge about microscopic details of the dopant distribution in the catalytic layer and the particular effect of dopants on the activity of the SCR reaction is still limited, and experiments alone have difficulties identifying the synergetic effects of dopants.[29] Theoretical modeling based on quantum chemistry calculations can assist in clarifying the role of dopants, yielding a qualitative understanding and building a design strategy for optimizing the SCR activity. However, theoretical studies based on density functional theory (DFT) have not led to a consensus yet. Instead they have focused on controversial mechanisms, such as NO and NO_2 involved SCR mechanisms[30–32] or the question of whether NH_3 mainly adsorbs either on Brønsted base sites (V-OH) or Lewis acid sites (Vanadium site).[33–38] Only a few computational studies[39–41] tackle the influence of the dopants on the activation and deactivation of the catalyst, e.g., by studying Hg and Pb poisoning.

Therefore a systematic theoretical study covering the whole SCR reaction path could be very beneficial to understand the role of dopants in SCR activity. Here we employ

a general parameter to describe the properties of oxide catalysts. Doping a metal oxide catalyst by another metal changes the stoichiometry of the oxide, in particular when the preferred oxidation state of the dopant is different from that of the metal element of the host oxide. This change will also influence the stability of the catalyst. Thus, stoichiometry might be a suitable parameter or descriptor to screen oxide catalysts with better reactivity and stability. Whereas the reactivity can be assessed in first-principles electronic structure calculations by identifying reaction mechanisms, including activation barrier heights,[42,43] the relative stability of different catalyst structures, compositions, and stoichiometry under operating conditions can be evaluated employing grand-canonical schemes.[8,44–47]

Often, stoichiometric configurations are among the most stable structures. A large deviation from the stoichiometric condition leads to unstable configurations unless a particular reconstruction lowers the energy. Thus, stoichiometric configurations will typically show high longevity. Still, as noted in our previous study,[8] a higher reactivity can be found for non-stoichiometric oxide configurations, where the adsorption of a reactant can restore the stoichiometry and thus gain additional energy by stabilizing the oxide.

This paper will explore the activity and thermodynamic stability of doped SCR catalysts using periodic first-principles electronic structure calculations. The oxide configurations considered in this study are based on the W-doped vanadia configurations on a titania substrate studied in our previous work.[8] The metal oxide catalysts are further tailored by replacing W with dopant elements such as W, Ce, Zr, Nb, or Mo. As proposed in our previous work,[8] the stoichiometry of the catalyst is not only critical with respect to the surface stability but also with regard to the local reactivity as it determines the Lewis acidity of the dangling vanadyl groups of the catalyst layer. Here we will further stress the relationship between the stoichiometry of oxide catalysts and the local electron-filling of the vanadia layer, using periodic first-principles electronic structure calculations. Typically, it is assumed that the surface stoichiometry of the vanadia layer is governed by the dopant concentration and the chosen dopant species. We will show that it is further affected by the

ionic bonding strength between the support and catalyst layer. Finally, we will demonstrate that the surface stoichiometry of the doped vanadia layer can act as a good descriptor for the redox property in each elementary reaction step.

Computational details

Spin-polarized periodical DFT calculations were performed[48] using the Vienna ab initio simulation package VASP[49–51] together with the projected augmented wave (PAW) method.[52,53] Exchange-correlation effects were considered within the generalized gradient approximation (GGA) using the Perdew-Burke-Ernzerhof (PBE) functional[54] and dispersion effects were included based on the DFT-D3 method.[55] The wave functions were expanded using a plane wave basis set with a kinetic cut-off energy of 400 eV. On-site Coulomb interactions were taken into account through the DFT+U approach[56,57] to treat the highly localized 3d, 4d, and 4f states. We employed the following semi-empirical parameters $U-J$: Ti (3d, 3.5 eV[58]), V (3d, 3.0 eV[59]), W (4d, 6.2 eV[60]), Nb (4d, 4.0 eV[61]), Zr (4d, 4.0 eV[62,63]), Mo (4d, 6.3 eV[64]), and Ce (4f state, 5.0 eV[65,66]).

We prepared the catalyst configurations using tungsten-doped vanadia layer on a TiO_2 substrate consisting of eight TiO_2 layers with a (001) surface termination. Note that there is well-known (1×4) admolecule (ADM) surface reconstruction[67] for TiO_2(001). However, in our previous study we found that overall the $W_xV_yO_z$ layers on the unreconstructed TiO_2 support are more stable than the corresponding layers on the ADM-reconstructed TiO_2 support.Therefore here we only consider layers on the (1×4) unreconstructed support. A vacuum layer of 25 Å was chosen to separate the surface slabs to avoid any spurious interactions normal to the surface. The surface structures were assumed to reach convergence when the forces on all relaxed atoms became smaller than 0.03 eV/Å. A dipole correction was included to compensate for the interaction between surface dipoles and their periodic images. A k-point mesh[68] of $3 \times 3 \times 1$ was employed to approximate the integral over the first Brillouin

zone of the 1×3 unit cell. Convergence tests confirmed that energy changes upon using a more dense $5 \times 5 \times 1$ k-point mesh are negligible. The convergence of the computational results with respect to the k-point sampling for other unit cell sizes was equally carefully checked.

To evaluate the surface stability under experimental operating conditions,[69] we derived the surface energy $\gamma(T, p)$ as a function of temperature T and pressure p within the grand-canonical ab initio thermodynamics scheme:[44,47]

$$\gamma(T, p) = \frac{1}{2A} \left[G(T, p, N_{\text{Ti}}, N_{\text{V}}, N_{\text{W}}, N_{\text{O}}) - \sum_i N_i \mu_i \right], \tag{1}$$

where A and G are the surface area and the Gibbs free energy, respectively, of a configuration consisting of N_i atoms of species i where i stands for Ti, V, W, or O atoms. μ_i represents the chemical potential of each species i. As a reference, we have taken the bulk phases of TiO_2, V_2O_5 and WO_3 in thermodynamic equilibrium with gas-phase O_2 under varying conditions. Thus, the chemical potentials of Ti, V and W are expressed as $\mu_{\text{Ti}} = \mu_{\text{TiO}_2}^{(bulk)} - 2\mu_{\text{O}}$, $\mu_{\text{V}} = (\mu_{\text{V}_2\text{O}_5}^{(bulk)} - 5\mu_{\text{O}})/2$ and $\mu_{\text{W}} = \mu_{\text{WO}_3}^{(bulk)} - 3\mu_{\text{O}}$, respectively. The chemical potential of oxygen $\mu_{\text{O}}(T, p)$ can be expressed as $\frac{1}{2}\mu_{\text{O}_2}(T, p)$, i.e. with respect to dioxygen gas at temperature T and pressure p. The O-rich limit of μ_{O_2} is assumed to correspond to gas-phase O_2 under the standard conditions, and the O-poor limit corresponds to metallic Ti, VO_2 and WO_2 formation, respectively, i.e. the heat of formation is $-\Delta H_f = \mu_{\text{TiO}_2}^{(bulk)} - \mu_{\text{Ti}}^{(bulk)} - \mu_{\text{O}}$ (-8.50 eV), $\mu_{\text{V}_2\text{O}_5}^{(bulk)} - 2\mu_{\text{VO}_2}^{(bulk)} - \mu_{\text{O}}$ (-13.01 eV) and $\mu_{\text{WO}_3}^{(bulk)} - \mu_{\text{WO}_2}^{(bulk)} - \mu_{\text{O}}$ (-7.18 eV). As the limit of μ_{O} for VO_2 and metallic Ti formation is beyond the range that allows WO_2 formation, the O-poor limit for $W_xO_yO_z/TiO_2$ is given by the one for WO_2 formation.

The adsorption energy of the considered molecules has been calculated with respect to the chemical potentials of the reference molecules μ_{NH_3}, μ_{NO}, $\mu_{\text{H}_2\text{O}}$, and μ_{O_2}. For reaction intermediates, the following references have been chosen: $\mu_{\text{NH}_2} = \mu_{\text{NH}_3} - \mu_{\text{H}}$, and $\mu_{\text{NH}_2\text{NO}} = \mu_{\text{NH}_2} + \mu_{\text{NO}}$ with $\mu_{\text{H}} = (\mu_{\text{H}_2\text{O}} - \mu_{\text{O}_2}/2)/2$. The adsorption energy of the adsorbate species

mol is then determined according to

$$E_{ads}^{mol} = E_{mol/cata} - E_{cata} - \mu_{\mathrm{mol}} \ , \tag{2}$$

where $E_{mol/cata}$ and E_{cata} are the energies of the model catalyst with/without the adsorbate *mol*. The chemical potential of any adsorbate *mol* at temperature T and partial pressure p_{mol} is given by

$$\mu_{mol}(T,p) = \mu_{mol}(T,p^{\ominus}) + RT\ln(p_{mol}/p^{\ominus}) \ , \tag{3}$$

where $\mu_{mol}(T,p^{\ominus})$ is the gas-phase energy of adsorbate *mol* at temperature T and standard atmospheric pressure $p^{\ominus}$. The temperature dependence of $\mu_{mol}(T,p^{\ominus})$ has been taken from the NIST-JANAF thermodynamic table.[70] For the chemical potentials of NH_3 and NO, the enthalpic temperature correction was ignored as this contribution is usually hardly changed upon adsorption. With respect to the partial pressures, we have chosen the following typical experimental conditions: p_{O_2}=0.1 atm, p_{N_2}=0.85 atm, p_{H_2O}=0.05 atm, p_{NH_3}, p_{NO}=1000 ppm at 600 K.[69]

The general nudged elastic band (NEB) method[71] with four images was employed to determine the activation barriers of the considered chemical reactions. To reduce the computational cost of the numerically demanding NEB calculations, we removed the four bottom layers of the support from the slab and fixed the bottom layer. The activation barrier E_a and reaction energy ΔH were calculated according to $E_a = E_{\mathrm{TS}} - E_{\mathrm{IS}}$ and $\Delta H = E_{\mathrm{FS}} - E_{\mathrm{IS}}$, respectively, where E_{IS}, E_{TS}, and E_{FS} are the energies of the initial state (IS), the transition state (TS) and the final state (FS) of the reaction. In order to estimate the charge distribution in the doped vanadia layers, we have employed a charge partitioning method.[72,73] Note that charge partitioning schemes are crude approximations, and different schemes may give different numbers as there is no strict definition regarding which electrons should be associated with which atoms. Still trends in the changes of partitioned charge to the system should be robust, independent of the particular choice of the partitioning scheme.

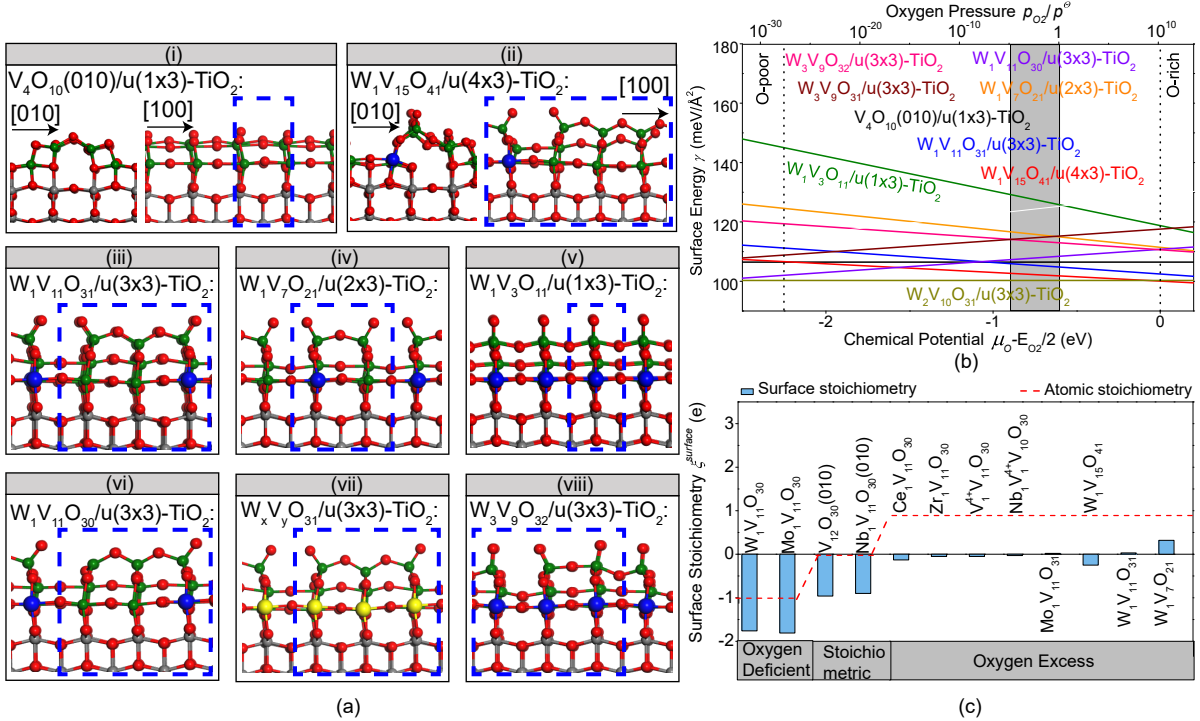# Substitutional doping of the V_2O_5/TiO_2 catalyst

Figure 1: (a) Side view of the structures of the considered $W_xV_yO_z/TiO_2$ catalysts along different directions, as indicated in the specific panel. The corresponding unit cells used for configurations (i) to (viii) are indicated by the blue dotted lines. The O atoms are colored in red, vanadium in green, tungsten in blue and the Ti atoms in gray. The light yellow atoms represent either vanadium or a dopant, (b) Surface energies for structures in (a) as a function of the chemical potential of oxygen. The gray shadowed area refers to the experimental growth condition of the catalyst (p_{O_2}=0.1 atm at 600 K). (c) Surface stoichiometry of the $M_xV_yO_z$ layers (M=W, Mo, V, Nb, Zr and Ce) for various atomic stoichiometry, concentrations and dopant species. The expected value (red dashed line) is derived from the nominal stoichiometry based on the standard oxidation states of the involved elements whereas the blue bars are determined according to Eq. 4 (see text).

As proposed in our previous work,[8] the high SCR performance of the commercial W-doped vanadia catalysts is closely related to the stoichiometry of the tungsta-vanadia layer which determines the formation of active terminal vanadyl (V=O) configurations. Stable vanadia surfaces are flat and smooth without any dangling oxygen groups, as depicted in configuration (i) of Fig. 1a. Only adequate substitutional doping of vanadia by other metals can create stable and active vanadyl configurations on the surface. For example, tungsten,

with its formal oxidation number $+6$, attracts an additional oxygen atom to the surface upon substituting vanadium with its formal oxidation number $+5$, as illustrated by configuration (v) in Fig. 1a, and creates a dangling oxygen configuration which, however, is not fully saturated.

However, increasing vanadyl coverage does not simply guarantee higher catalytic activity. The activation of the NO capture requires a vanadium site for NH_3 adsorption and an active dangling oxygen bond configuration at a neighboring site for breaking the N-H bond to produce the NH_2 intermediate, as realized by configuration (vi) in Fig. 1a. Therefore, better SCR performance demands further optimization of the active vanadyl distribution and coverage on vanadia. In this work, we primarily focus on the influence of dopants such as Ce, Zr, Nb, W, and Mo on the formation, distribution, and coverage of active vanadyl species.

Based on the structural analysis of the surface terminations studied in Ref.,[8] we first study extended stoichiometric vanadia areas by considering larger unit cells along the [100] direction,[8] as shown in configuration (i) of Fig. 1a. Isolated tungsten atoms in the vanadia layer are introduced by substitutional doping together with one additional oxygen, which creates one-electron deficient W-doped vanadia layers $W_1V_7O_{21}$ (configuration (iv) in Fig. 1a), $W_1V_{11}O_{31}$ (configuration (iii)), and $W_1V_{15}O_{41}$ (configuration (ii)) within the $u(2 \times 3)$, $u(3 \times 3)$, $u(4 \times 3)$ unit cells, respectively, of the $TiO_2(001)$ support. As shown in Fig. 1a, the W doping lifts off a part of the uppermost layer of vanadia and breaks one lateral V-O bond of the V atom with the dangling oxygen after structural optimization. The structural change leads to the formation of a vanadia row with dangling oxygen atoms at the surface. An isolated W leads to the formation of a pair of neighboring dangling oxygen atoms in practice.

Secondly, we consider W atoms at neighboring sites by replacing more than one V atom in the $V_{12}O_{30}$ layer on $u(3 \times 3)$-TiO_2. The resulting configurations (vii) $W_2V_{10}O_{31}$ and (viii) $W_3V_9O_{32}$ in Fig. 1a correspond to stoichiometric and oxygen-excess configurations,

respectively. The $W_3V_9O_{32}$ layer shows only one extra dangling oxygen in the middle of the vanadyl pair compared with the configuration of $W_2V_{10}O_{31}$. Finally, we create oxygen-deficient configurations by removing one oxygen from the $W_1V_{11}O_{31}$ and $W_3V_9O_{32}$ layers. In the oxygen-deficient $W_1V_{11}O_{30}$ configuration (vi) in Fig. 1a, one exposed vanadium atom is neighboring a site with dangling oxygen, which is ideal for NH_3 adsorption. Note that $W_1V_9O_{31}$, $W_2V_{10}O_{31}$, and $W_3V_9O_{31}$ layers (configuration (vii) $W_xV_yO_{31}$ in Fig. 1a) end up with a similar dangling oxygen configuration but correspond to different atomic stoichiometry. These examples illustrate how the dopant concentration and distribution can influence the electronic properties of a dangling oxygen configuration. Notably, all the surfaces mentioned above were actually terminated with isolated vanadyl configurations. In contrast, in $W_1V_3O_{11}$ (configuration (v) in Fig. 1a), a periodic arrangement of dangling oxygen bonds appears.

Fig. 1b shows the surface energies of W-doped vanadia layers as a function of the oxygen chemical potential. Interestingly, the electron-deficient $W_1V_{11}O_{31}$ configuration (blue line) has a surface energy similar to the one of the stoichiometric V_4O_{10} layer (black line) at $\mu_O > -1$ eV. The $W_1V_{15}O_{41}$ configuration (red line) even displays a lower surface energy with a value close to the stoichiometric W-doped vanadia $W_2V_{10}O_{31}$ configuration (brown line) which exhibits the lowest surface energy in Fig. 1b. Having a low W concentration resulting in $W_1V_{11}O_{31}$ and $W_1V_{15}O_{41}$ structures further lowers the surface energy significantly compared to $W_1V_3O_{11}$ (green line) and $W_1V_7O_{21}$ (orange line), and stabilizes the electron-deficient vanadia layer which may coexist with the WO_3 phase under operating conditions (grey area in Fig. 1b). We note that the $W_1V_3O_{11}$ configuration (green line) has the highest density of dangling oxygen groups which makes this surface termination energetically rather costly. Hence surface structures with an extended arrangement of dangling oxygen groups are rather unlikely to occur. The higher stability of isolated vanadyl configurations on the surface is in good agreement with the experimental findings of dispersing distribution of vanadyls.[74,75] In addition, Grünert et al.[76] proposed mixed vanadium and tungsten phases and a direct

promotional effect of neighboring vanadium and tungsten sites for an enhanced SCR activity.

The local reactivity of oxide catalysts can be related to the stoichiometry of the active portion of the catalyst,[8] which in the case considered here corresponds to the doped $M_xV_yO_z$ vanadia layer. In this work, we will check whether indeed the stoichiometry of the whole surface layer can be used to estimate the activity of the catalyst. In other words, we will scrutinize whether the stoichiometry of a surface is an adequate descriptor for its catalytic activity.

Our previous work[8] has demonstrated that the formal stoichiometry determined by simply counting the oxidation numbers of the elements can be used to estimate the catalytic activity towards H adsorption. Oxygen-deficient structures are associated with energetically favorable hydrogen adsorption whereas on oxygen-excess or stoichiometric configurations there is an energy cost to adsorb hydrogen. However, H adsorption energies can also vary as a function of the dopant species and concentration within the same formal stoichiometry, as will be discussed below. Therefore we will here introduce a more general definition of local stoichiometry. Actually in the determination of the stoichiometry of a surface layer, one has to take into account that the surface layer might overall not be charge neutral due to some charge transfer from the support.[77] Hence, in order to estimate the charge distribution in the doped vanadia layers, we have employed a charge partitioning method.[72,73] Note that typically different charge partioning schemes give different numbers as there is no strict definition with respect to the fact which electrons should be associated with which atoms. Still trends in the charge partioning upon changes to the system should be robust, independent of the particular choice of the particular charge partitioning scheme.

Indeed, the charge partitioning analysis demonstrates that the doped vanadia layers become negatively charged due to electron transfer from the titania support in agreement with experimental observations.[78] The sum of the atomic charges in the titania layers is positive by about one elementary charge unit, which indicates that the doped vanadia layers are more electron-rich than expected from the formal stoichiometry (dashed line in Fig. 1c).

11

Hence in order to derive the generalized surface stoichiometry ξ^{surface}, the charge transfer at the interface $\xi^{\text{interface}}$ needs to be accounted for on top of the formal stoichiometry based on the standard oxidation number analysis ξ^{cata}. However, specific local charge rearrangements within the catalyst layer can also induce a change in the surface stoichiometry. For example, when a vanadyl group is formed by breaking a V-O bond at the flat stoichiometric $V_{12}O_{30}(101)$ and $Nb_1V_{11}O_{30}(101)$ surfaces, the bond breaking causes a charge rearrangement to $V_1^{4+}V_{11}O_{30}$ and $Nb_1V_1^{4+}V_{10}O_{30}$. The reduction of one metal site leads to a higher electron deficiency in the remaining part of the vanadia layer, which can therefore accept electrons. Hence, the influence of the reduced metal site can be included by adding the contribution $\xi^{\text{reduction}} = 1$ to the surface stoichiometry of the configuration (ξ^{surface}). Furthermore, the charge exchange between reaction intermediates and the catalyst layer can also change the surface stoichiometry and influence the reactivity. Thus, the stoichiometry of each reaction step must include the contribution of reactants on the surface ξ^{reactant} too. The effective generalized surface stoichiometry is then given by

$$\xi^{\text{surface}} = \xi^{\text{cata}} + \xi^{\text{interface}} + \xi^{\text{reduction}} + \xi^{\text{reactant}} \ . \tag{4}$$
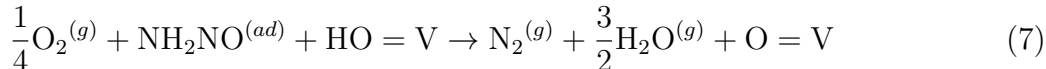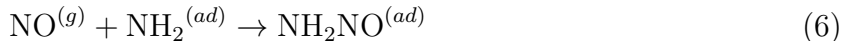
In Fig. 1c, the blue bars depict the generalized surface stoichiometry ξ^{surface} of the $M_xV_yO_z$ layer, whereas the red dashed line corresponds to the formal stoichiometry ξ^{cata}. As demonstrated in Fig. 1c, by counting all considered contributions, the flat vanadia $V_{12}O_{30}(101)$ surface is already non-stoichiometric with $\xi^{\text{surface}} \approx -1 \ e$.

The creation of the electron-deficient dangling oxygen bonds in oxygen-excess configurations leads to a positive ξ^{surface} of the vanadia when the dangling oxygen coverage is high enough ($\geq 2/3$), as shown for the case of $W_1V_7O_{21}$. In the case of the $W_1V_{11}O_{31}$ layer with a vanadyl coverage of $2/3$, ξ^{surface} is weakly positive and close to zero for the stoichiometric configuration. On the other hand, although the oxygen-excess $W_1V_{15}O_{41}$ layer corresponds to an oxygen-excess configuration, ξ^{surface} becomes negative because of an electron transfer of

1.25 e from the support. Hence, a vanadyl configuration at the surface does not necessarily guarantee a catalytically active electron-deficient state that can readily accept electrons.

SCR reaction on doped vanadia catalysts

The generally accepted SCR mechanism consists of three crucial steps, i.e., the activation of the catalyst by NH_3 adsorption and dissociation to NH_2, N-N coupling by NO adsorption, and the recovery of the catalyst by forming N_2 and water:

$$NH_3^{(g)} + O = V \rightarrow NH_2^{(ad)} + HO = V \tag{5}$$

$$NO^{(g)} + NH_2^{(ad)} \rightarrow NH_2NO^{(ad)} \tag{6}$$

$$\frac{1}{4}O_2^{(g)} + NH_2NO^{(ad)} + HO = V \rightarrow N_2^{(g)} + \frac{3}{2}H_2O^{(g)} + O = V \tag{7}$$

In the following, we will discuss the influence of dopants on these steps subsequently in terms of the surface stoichiometry ξ^{surface}.

NH_3 adsorption and catalyst activation

Ammonia can get adsorbed at either Lewis acid (V) or Brønsted acid (V-OH) sites on the vanadia layer. Herein, we mainly focus on NH_3 adsorption at the Lewis acid site. Figure 2 illustrates various possible scenarios of such a NH_3 adsorption at a Lewis acid site. In these scenarios, a dopant M=Mo, W, Ce, Zr, and Nb has replaced one of the V atoms at an A, B, C, or D site yielding a $M_1V_{11}O_z$ catalyst layer. Furthermore, additional neighboring vanadium sites, including the E and F sites, also become replaced by W resulting in $M_2V_{10}O_{31}$ and $M_3V_9O_z$ layers, as depicted in Fig. 2. Figure 2a illustrates NH_3 adsorption at an exposed vanadium site, which corresponds to direct adsorption and which we denote by Adsorption I.
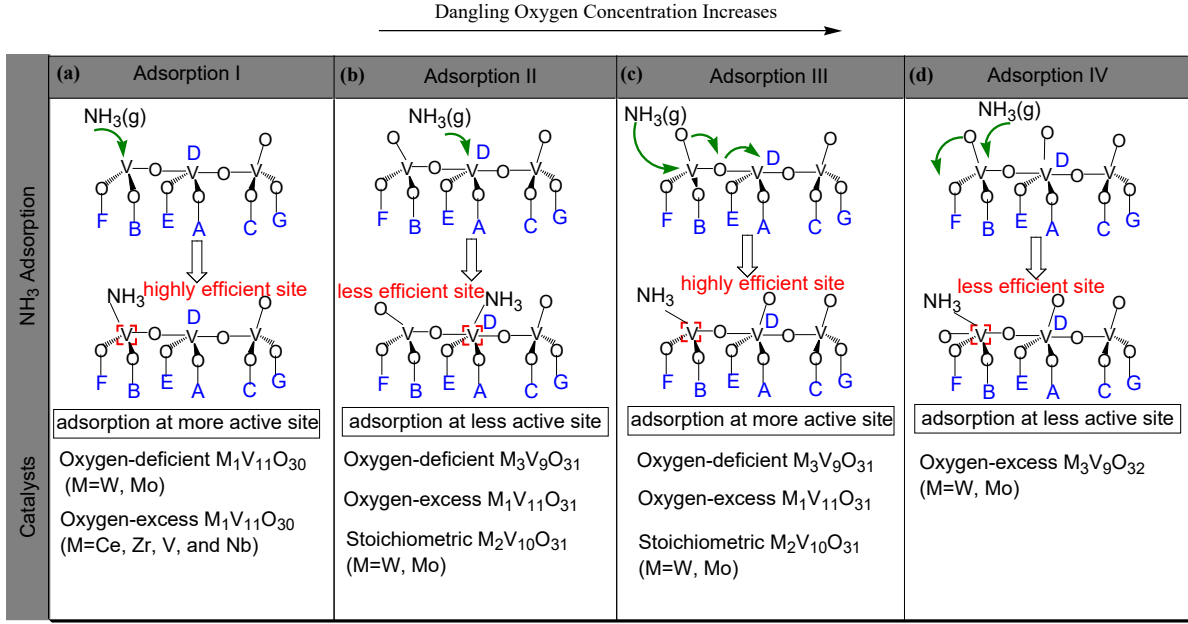
Figure 2: Mechanisms of NH_3 adsorption on doped vanadia $M_xV_yO_z$ (M refers to dopant).

Table 1: NH_3 adsorption energies in eV on $M_xV_yO_z/TiO_2$ (M=dopant)

Adsorption Type	Catalysts	Site A	Site B	Site C	Site D
	$W_1V_{11}O_{30}$	-1.69	-1.75	-1.66	-1.77
	$Mo_1V_{11}O_{30}$	-1.71	-1.73	-1.66	-1.77
I	$Ce_1V_{11}O_{30}$	-2.28	-2.25	-2.34	-0.73
	$Zr_1V_{11}O_{30}$	-2.26	-2.47	-2.40	-0.87
	$Nb_1V_{11}O_{30}$	-2.41	-2.64	-2.42	-1.94
II	$W_1V_{11}O_{31}$	-0.32	-0.28	-0.28	-0.41
III	$W_1V_{11}O_{31}$	-0.21	0.16	0.03	-0.50
	$Mo_1V_{11}O_{31}$	-0.11	0.26	0.13	-0.28

Adsorption Type	Catalysts	Sites B and C	Sites A and B	Sites A and C	Sites B and D
III	$W_2V_{10}O_{31}$	0.38	0.05	-0.14	-0.12

Adsorption Type	Catalysts	Sites A, B and C	Sites A, B and E	Sites A, C and F	Sites B, C and D
III	$W_3V_9O_{31}$	-0.52	-0.22	0.39	-1.72
IV	$W_3V_9O_{32}$	-0.24	0.00	-0.14	-0.41

Site M (M=A-F) means the substitutional vanadium site by dopant in Fig. 2.
Adsorption type refers to the adsorption I-IV in Fig. 2.

Based on experiments,[79] the exposed coordinately unsaturated V sites are considered to be more active for the subsequent reactions compared with the coordinately saturated V sites. The optimized configurations exhibit elongated N-H bonds by 4% at the exposed site, which is an activated configuration for NH_3 dissociation. We note that despite the same atomic

14

configuration, the formal stoichiometry can become different through the selection of specific dopants. In the case of the $M_1V_{11}O_{30}$ layer, W and Mo doping leads to an oxygen-deficient situation, whereas it results in an oxygen-excess configuration for Ce, Zr, V, and Nb doping. When pairs of dangling oxygen bonds exist in $M_xV_yO_{31}$ configurations, as illustrated in Fig. 2b, NH_3 adsorbs at one of the coordinately saturated V sites, which are less efficient for further reactions (Adsorption II), as discussed above. However, the adsorption of NH_3 can lead to a rearrangement of the dangling oxygen atom to the neighboring vanadium site, as shown in Fig. 2c, then the molecule can bind to the highly efficient vanadium site mentioned above (Adsorption III). The Adsorption scenarios II and III can occur on W- or Mo-doped vanadia, and the dopant concentration determines the atomic stoichiometry of the catalyst, leading to oxygen-deficient ($M_3V_9O_{31}$), oxygen-excess ($M_1V_{11}O_{31}$), and stoichiometric ($M_2V_{10}O_{31}$) configurations, respectively. In the Adsorption IV scenario for $M_3V_9O_{32}$ configurations (Fig. 2d), all vanadium sites at the surface are covered by dangling oxygen atoms. Then, NH_3 can only adsorb at a vanadium site through catalyst deformation by the bending of an O=V bond. Such a high coverage of dangling oxygen atoms only occurs at high W or Mo concentrations in oxygen-excess configurations.

Table 1 lists the NH_3 adsorption energies derived according to Eq. 2 for various dopant species and configurations. The energy gain depends on the particular dopant species but is only weakly sensitive to the specific position of the dopant. Overall, tbe adsorption energies have values of about -2 eV for Adsorption scenario I. For Adsorption scenarios II, III, and IV, the binding energies are smaller than for Adsorption scenario I by around 1.5 eV because of the significant structural change of the catalyst upon adsorption. In Fig. 3, we compare the change in the NH_3 adsorption energy (blue bar) and the surface stoichiometry ξ^{surface} (red bar) for varying dopant species (Mo, W, Nb, Zr, and Ce) for the most favorable adsorption process, namely Adsorption type I on $M_1V_{11}O_{30}$. Dopants located at the A, B, and C sites in the sublayer were considered as depicted in the three panels of Fig. 3. Doping at site D in the top layer was disregarded due to the large catalyst structural change
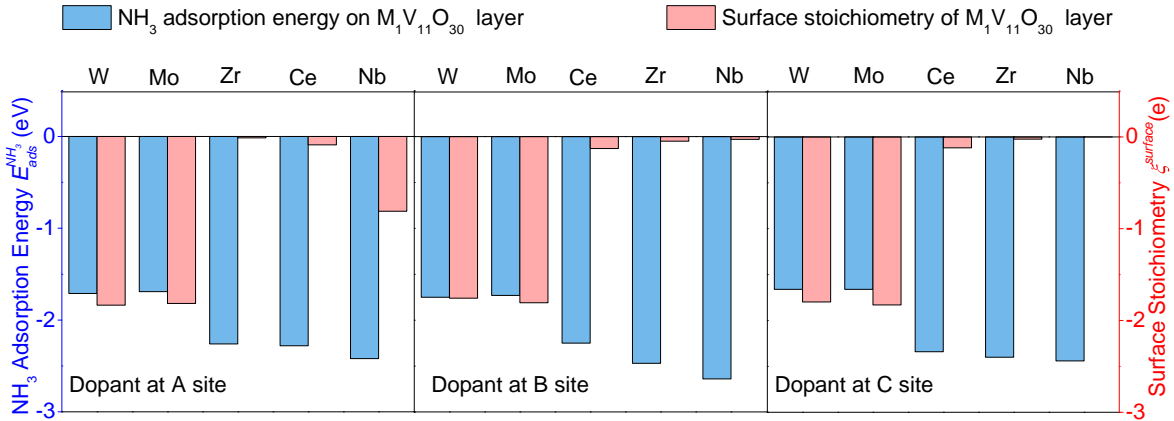
Figure 3: NH_3 adsorption energies and surface stoichiometry for $M_1V_{11}O_{30}$ layers (M= W, Mo, Zr, Ce and Nb) with dopant at A, B, and C sites established in Fig. 2.

induced by adsorption. Note the larger energy gain upon NH_3 adsorption at the oxygen-excess configurations, e.g., $Nb_1V_1^{4+}V_{10}O_{30}$, $Zr_1V_{11}O_{30}$ and $Ce_1V_{11}O_{30}$. In contrast, NH_3 adsorption at the oxygen-deficient configurations $Mo_1V_{11}O_{30}$ and $W_1V_{11}O_{30}$ is energetically less favorable. A less negative surface stoichiometry $\xi^{surface}$ is in general associated with a stronger NH_3 bonding, i.e., $\xi^{surface}$ and the adsorption energy are apparently anti-correlated. The trend is the same for H adsorption[8] as NH_3 adsorption is accompanied by an electron transfer from NH_3 to the surface. This electron transfer leads to an elongated N-H bond after NH_3 adsorption. Overall, more electron-deficient surfaces favor NH_3 adsorption. However, we find that Nb doping at site A leads to a more negative surface stoichiometry $\xi^{surface}$ than Zn and Ce doping but is associated with a larger gain in NH_3 adsorption energy. This means that the larger structural change of the vanadia layer upon Nb doping results in a more open structure, which causes a stronger NH_3 binding.

NH_3 dissociation and O-H formation

The adsorbed NH_3 dissociates to NH_2 by breaking one N-H bond and forming an O-H bond at the neighboring dangling oxygen bond site. The charge analysis shows that NH_3 adsorption is associated with an electron transfer of about $0.2\ e$ to the vanadia layer before
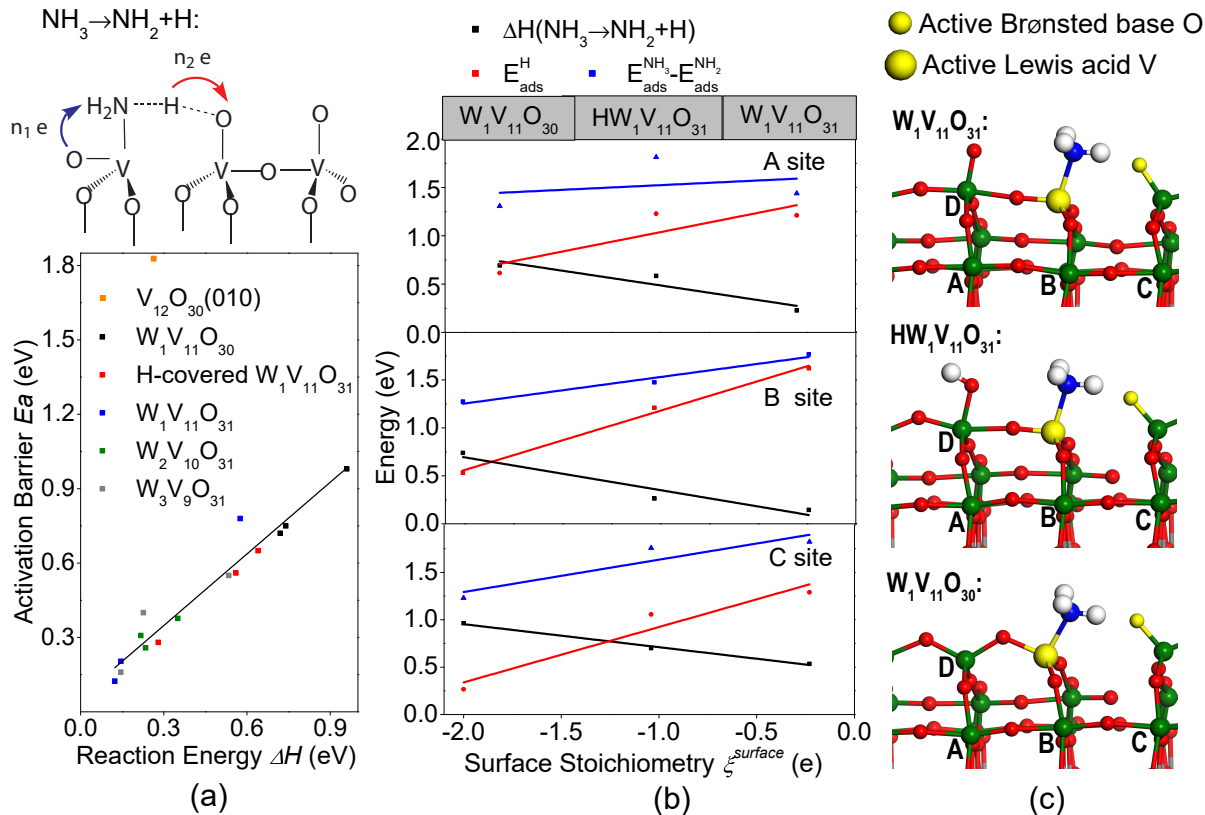
16

Figure 4: NH$_3$ dissociation for various sites on W-doped vanadia surfaces. (a) Illustration of NH$_3$ dissociation mechanism and the relationship between activation barriers and reaction energies of NH$_3$ dissociation. (b) Decomposition of the reaction energy at H$_x$W$_1$V$_{11}$O$_z$ model catalyst layers. Black dots: reaction energy ΔH of NH$_3$ dissociative adsorption; red dots: hydrogen adsorption energy E_{ads}^{H}; blue dots: difference between NH$_3$ and NH$_2$ adsorption energies $E_{ads}^{NH_3} - E_{ads}^{NH_2}$. The lines serve as a guide to the eye. (c) Illustration of the NH$_3$ configuration on the H$_x$W$_1$V$_{11}$O$_z$ model catalyst layers corresponding to the initial structure before NH$_3$ dissociation.

N-H bond breaking. As sketched in Fig. 4a, the N-H bond breaking leads to a simultaneous electron transfer from vanadia to NH$_2$ ($n_1\,e \approx 0.13\,e$) and from the hydrogen atom to vanadia ($n_2\,e \approx 0.10\,e$). Note that the magnitude of $n_1\,e$ and $n_2\,e$ is comparable, i.e., the electron transfer from vanadia to NH$_2$ is roughly compensated by the back-transfer from the hydrogen to the vanadia. Two surface sites are involved in this reaction, an exposed Lewis acid V site that activates NH$_3$ dissociation to NH$_2$, and a Brønsted base V=O site that captures the H atom upon NH$_3$ dissociation, as illustrated in Fig. 4a. If no V=O group is available to attract the H atom, as for example on the flat vanadia V$_{12}$O$_{30}$(010) surface, then the activation

barrier for NH_3 dissociation will become rather large (1.83 eV on $V_{12}O_{30}$(010), orange dot in Fig. 4a), because of the high cost of breaking one V-O bond at the surface. Hence W doping, which creates dangling oxygen bonds at the surface, thus lowers the dissociation barrier considerably. In particular, when a V=O site is available to capture the H atom at the neighboring site, the potential energy surface becomes relatively flat after the transition state of N-H bond breaking. Then, the reaction energy and the activation barrier are almost identical, as shown in Fig. 4a, which displays the correlation between reaction energies and activation barriers of NH_3 dissociation on W-doped vanadia for various tungsten distributions and concentrations. This corresponds to a kind of Brønsted-Evans-Polanyi (BEP) relation.[80] Hence the facile activation of NH_3 requires a suitable atomic configuration with an exposed V site neighboring a dangling oxygen bond site (Adsorption scenarios I and III in Fig. 2a and c). At the same time, this means that the backward reaction can occur without any considerable barrier for these configurations. Conserquently, there might be an oscillating behavior of H exchange between the Lewis acid and Brønsted base sites.

In the following, we particularly focus on three types of model catalyst layers, shown in Fig. 4c, to disentangle the contributions of surface stoichiometry and dopant distribution. The layers correspond to vanadia with a low doping concentration and similar local structures of Lewis acid and Brønsted base sites. The surface stoichiometries ξ^{surface} of NH_3 adsorbed on the $W_1V_{11}O_{31}$, H-covered $W_1V_{11}O_{31}$ and $W_1V_{11}O_{30}$ layers, denoted by $H_xW_1V_{11}O_z$, are about -0.2 e, -1 e, and -2 e, respectively. In practice, four V sites are available for W-doping, as shown in Fig. 4c. However, ammonia adsorption becomes favorable by 1 eV for W-doping in the sublayer (A, B, and C sites) compared to the top layer (D site). Moreover, W-doping at the D site increases the reaction energy by 0.13, 0.63, and 1.28 eV compared to doping in the sublayer. Thus, W-doping at the D site is not favorable for the SCR, so that we mainly consider W dopant at the sublayer V sites A, B, and C.

The black dots in Fig. 4b represent the reaction energy ΔH of NH_3 dissociation. In general, the reaction energy decreases linearly as a function of surface stoichiometry which is
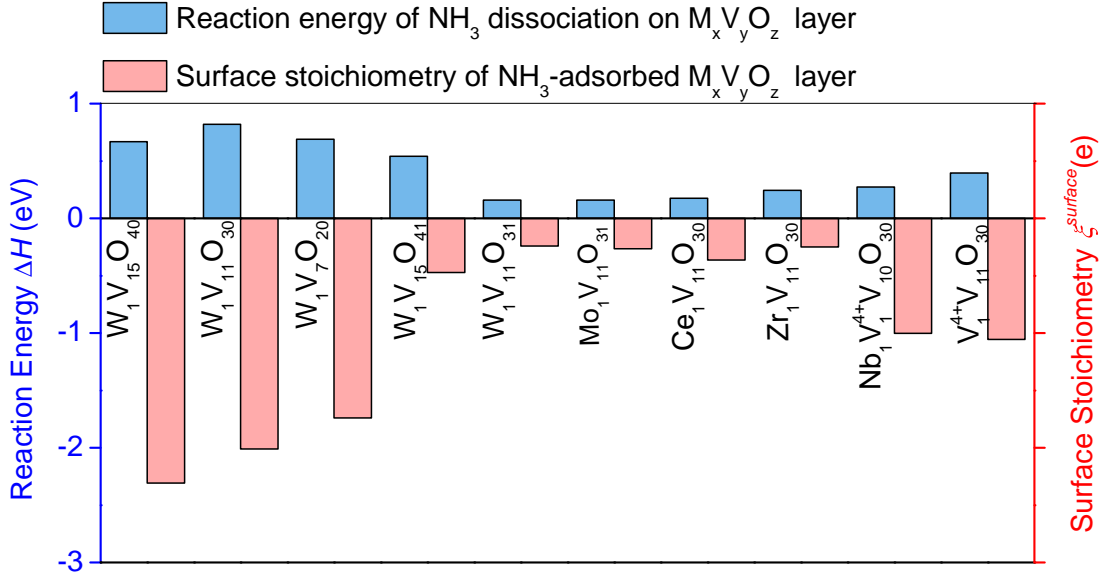
18

Figure 5: Reaction energies of NH_3 dissociation (blue bars) and surface stoichiometry (red bars) for NH_3 adsorbed on $M_xV_yO_z$ layers (M= W, Mo, Zr, Ce, V and Nb) with the dopant at the B site, as illustrated in Fig. 2.

also associated with a lower activation barrier. To assess the contribution of the Lewis acid and Brønsted base sites to the overall reaction energy, we decompose the reaction energy $(\Delta H = E_{ads}^{\mathrm{H}} - (E_{ads}^{\mathrm{NH_3}} - E_{ads}^{\mathrm{NH_2}}))$ into the difference of the adsorption energy change from NH_2 to NH_3 at the Lewis acid site (blue dots, $E_{ads}^{\mathrm{NH_3}} - E_{ads}^{\mathrm{NH_2}}$) and the OH formation energy corresponding to the H adsorption energy at the Brønsted base site in the presence of NH_2 (red dots, E_{ads}^{H}), respectively. The increase in the OH formation energy (red line) exhibits a larger slope than the decrease in $E_{ads}^{\mathrm{NH_3}} - E_{ads}^{\mathrm{NH_2}}$ (blue line). Consequently, the increase in the H adsorption energy dominates the change in the reaction energy as a function of the surface stoichiometry ξ^{surface}. This is the reason why the trends in NH_3 dissociation activity and H adsorption energy as a function of the surface stochiometry ξ^{surface} are similar.

Fig. 5 displays the reaction energy ΔH of NH_3 dissociation and the surface stoichiometry ξ^{surface} for vanadia layers $M_xV_yO_z$ for various different dopant species. The dopant is located at the most active B site, and NH_3 adsorption types I and III (see Fig. 2) are considered.

Fig. 5 illustrates that in general a more positive surface stoichiometry ξ^{surface} leads to lower reaction energies of NH$_3$ dissociation. Recall, as just shown in Fig. 4b for H$_x$W$_1$V$_{11}$O$_z$ layers, that the OH formation energy dominates the reaction energy for NH$_3$ dissociation as a function of ξ^{surface}. The most electron-rich surfaces, W$_1$V$_{15}$O$_{40}$, W$_1$V$_{11}$O$_{30}$ and W$_1$V$_7$O$_{20}$, have an excess of about two electrons in the surface, which leads to the larger energy cost for NH$_3$ dissociation. The W$_1$V$_{15}$O$_{41}$ and W$_1$V$_{11}$O$_{31}$ configurations have a lower excess of less than one electron in the surface, which makes the dissociation of NH$_3$ energetically more favorable. Upon varying the dopant species from W to Mo, Ce, Zr, Nb, and V, the surface stoichiometry ξ^{surface} becomes more negative, i.e., there is a more pronounced electron-excess in the catalyst layers which makes NH$_3$ dissociation energetically less favorable. Ce, Mo, and W doping results in comparably low reaction energies indicating the potential to facilitate NH$_3$ dissociation. The W$_1$V$_{15}$O$_{40}$ layer at the far left in Fig. 5 corresponds to the most pronounced deviation in the obvious anti-correlation between surface stochiometry and the NH$_3$ dissociation reaction energy which is caused by a structural change into a more open configuration. Otherwise, Fig. 5 demonstrates that the surface stoichiometry ξ^{surface} acts as a reliable descriptor for the NH$_3$ reaction energy.

NO adsorption and N-N coupling

We now proceed to the next SCR reaction step, N-N coupling upon NO adsorption. After the dissociative adsorption of NH$_3$, the adsorbed NH$_2$ captures a NO molecule and forms the reaction intermediate NH$_x$NO ($x = 1, 2$) by forming an N-N bond which represents the precursor for the N$_2$ formation. We firstly probe the influence of the surface stoichiometry ξ^{surface} on this reaction step for W-doped vanadia layers considering the H$_x$W$_1$V$_{11}$O$_z$ layers mentioned above. Tungsten can replace a V atom at either the A, B, or C site, as illustrated in the left panel of Fig. 6a. As NO does not directly adsorb on vanadia, the reaction energy for N-N coupling is calculated with respect to adsorbed NH$_2$ and NO in the gas phase.

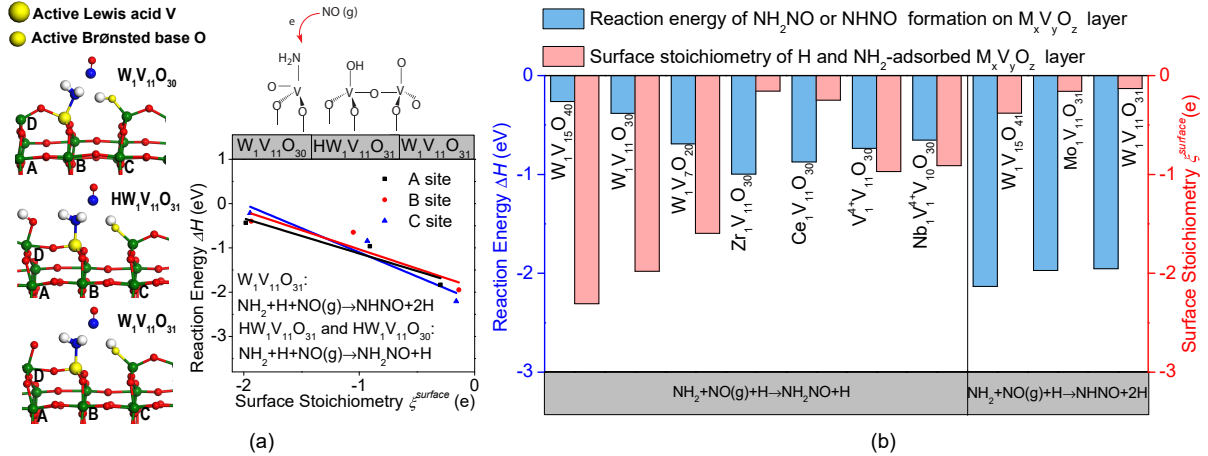Figure 6a demonstrates that there is linear relationship between the reaction energy for

Figure 6: NO adsorption and N-N coupling. (a) Mechanisms of electron transfer, the reaction energy and the surface stoichiometry ξ^{surface} for NH_xNO (x=1, 2) formation and the atomic reactant configuration with tungsten located at either the A, B or C site of the $H_xW_1V_{11}O_z$ model catalyst layers. (b) Reaction energies of N-N coupling and surface stoichiometry for dissociatively adsorbed NH_3 on $M_xV_yO_z$ layers (M= W, Mo, Zr, Ce, V and Nb) with the dopant at the B site, as illustrated in Fig. 2.

NH_xNO formation and the surface stoichiometry ξ^{surface} of the catalyst which only relatively weakly depends on the particular position of the dopant. On the oxygen-excess $W_1V_{11}O_{31}$ catalyst layer, an additional N-H bond breaking event after NH_2NO formation leads to adsorbed NHNO and H associated with an energy gain of about -2 eV. In contrast, on the stoichiometric and oxygen-deficient catalyst layers, NH_2NO is formed with a significantly smaller energy gain. As the unpaired electron of NO will be available for the interaction with the vanadia layer, as illustrated in Fig. 6a, the NO adsorption is more efficient on the electron-deficient vanadia layers with a more positive surface stoichiometry ξ^{surface}. We consider the most active dopant distribution (W at the B site) to analyze the relation between the

Table 2: The number of reduced vanadium (V^{4+}) sites at selected surfaces for various adsorbates.

Adsorbate	$W_1V_{11}O_{31}$	H-covered $W_1V_{11}O_{31}$	$W_1V_{11}O_{30}$
clean	0	0	1
NH_3	0	0	1
NH_2+H	0	0	1
NH_xNO(x=1, 2)	0	1	2

oxidation states of V and the surface stoichiometry ξ^{surface} of the vanadia layer. In Table 2, the number of reduced V^{4+} sites for clean and NH_3, NH_2+H, and NH_2NO covered $H_xW_1V_{11}O_z$ layers are listed. The surface stoichiometry ξ^{surface} of the $H_xW_1V_{11}O_z$ layers upon NH_2 and H adsorption roughly corresponds to $-0.2\,e$, $-1.0\,e$, and $-2.0\,e$, respectively. After NO adsorption, the vanadia layers attract more electrons from the reaction intermediates. However, only the H-covered $W_1V_{11}O_{31}$ and the $W_1V_{11}O_{30}$ layers form an additional reduced V^{4+} site upon NO adsorption, , as can be seen in the last line of Tab. 2. The reduction of vanadium is associated with a considerable energy cost which leads to smaller NO adsorption energies (see Fig. 6a) compared to the $W_1V_{11}O_{31}$ configuration, where all V sites are fully oxidized (V^{5+}) along the reaction path.

Fig. 6b compares the reaction energy of NH_xNO formation and corresponding surface stoichiometry ξ^{surface} using the layer configurations also considered in Fig. 5. NO adsorption selectively leads to either NH_2NO or $NHNO$ formation depending on the atomic configuration of the surface. On the oxygen-excess $W_1V_{11}O_{31}$, $Mo_1V_{11}O_{31}$ and $W_1V_{15}O_{41}$ layers, NO adsorption is accompanied by a N-H bond breaking event. When the NO molecule approaches the adsorbed NH_2 molecule, the neighboring dangling oxygen atom attracts one hydrogen atom and forms an OH group. The concerted reaction of N-N bond creation and N-H bond breaking leads to low activation barriers,[81] for example to an activation barreier of only $0.07\,\text{eV}$ on $W_1V_{11}O_{31}$. The corresponding significant reaction energies of -1.95, -2.13 and -1.97 eV for $W_1V_{11}O_{31}$, $W_1V_{15}O_{41}$, and $Mo_1V_{11}O_{31}$, respectively, allow the facile conversion of NH_2NO to $NHNO$ when dangling oxygen bonds are available at the neighboring sites. Thus, oxygen excess condition associated with a larger number of vanadyl groups at the surface are benefical for efficient NO capture and further N-H bond-breaking reactions. Without the presence of neighboring dangling oxygen sites, adsorbed non-dissociated NH_2NO will be created. The reaction energies of NH_2NO formation are in general smaller than those for NHNO formation. Moreover, upon variation of the dopant concentration and species, as shown in Fig. 6b, the reaction energy of NH_2NO formation becomes larger at layers with a

less negative surface stoichiometry ξ^{surface}. Hence, efficient NO capture is only possible at oxygen-excess configurations associated with more positive surface stoichiometries ξ^{surface}.

Catalyst recovery and energetics of H adsorption

The remaining step in the SCR reaction, N_2 formation from NH_xNO, is strongly exothermic. For example, the decomposition of NHNO on the $W_1V_{11}O_{31}$, $W_1V_{11}O_{41}$, and $Mo_1V_{11}O_{31}$ layers is associated with a reaction energy of about $-4\,\mathrm{eV}$. In contrast, the NH_2NO decomposition on $W_1V_{11}O_{30}$, $W_1V_{11}O_{40}$, and $Mo_1V_{11}O_{30}$ leads to a somewhat smaller energy gain of about $-2.5\,\mathrm{eV}$. Due to this large energy gain, N_2 formation and desorption occur rather spontaneously. After N_2 desorption, hydrogen can still remain on the surface in the form of surface hydroxyl groups. For the recovery of the catalyst, the hydrogen atoms need to be removed. In this section, we will focus on the energetics of the adsorbed hydrogen species. As we demonstrated previously,[8] O-H formation and hence strong hydrogen bonding is facile on electron-deficient (oxygen-excess) vanadia layers as the stoichiometry of the layer is recovered by accepting the electron from the hydrogen atom. Thus oxygen-excess is detrimental for the catalyst recovery whereas it is beneficial for NO-capture and the subsequent N_2 formation, as we just discussed above. This indicates that the preferred reaction conditions for catalyst activation and recovery are different. Thus, optimizing the H adsorption energy with respect to both catalyst activation and recovery is critical for an efficient catalyst operation.

Figure 7 displays the hydrogen adsorption energy and the surface stoichiometry ξ^{surface} for various doped $M_xV_yO_z$ layers. The electron-rich or oxygen-deficient layers with $\xi^{\mathrm{surface}} \approx -2\,e$ are associated with weak hydrogen bonding which becomes successively stronger for stoichiometric ($\xi^{\mathrm{surface}} \approx -1\,e$) and oxygen-excess ($\xi^{\mathrm{surface}} \approx 0$) doped vanadia layers. Mo and W doping even results in a positive surface stoichiometry ξ^{surface}, causing the largest energy gain upon hydrogen adsorption among the considered catalysts. Furthermore, there is also an influence of the dopant coverage on the H adsorption energy. Increasing the tungsten concentration from $W_1V_{15}O_{41}$ to $W_1V_{11}O_{31}$ and $W_1V_7O_{21}$ accompanied by an increase in
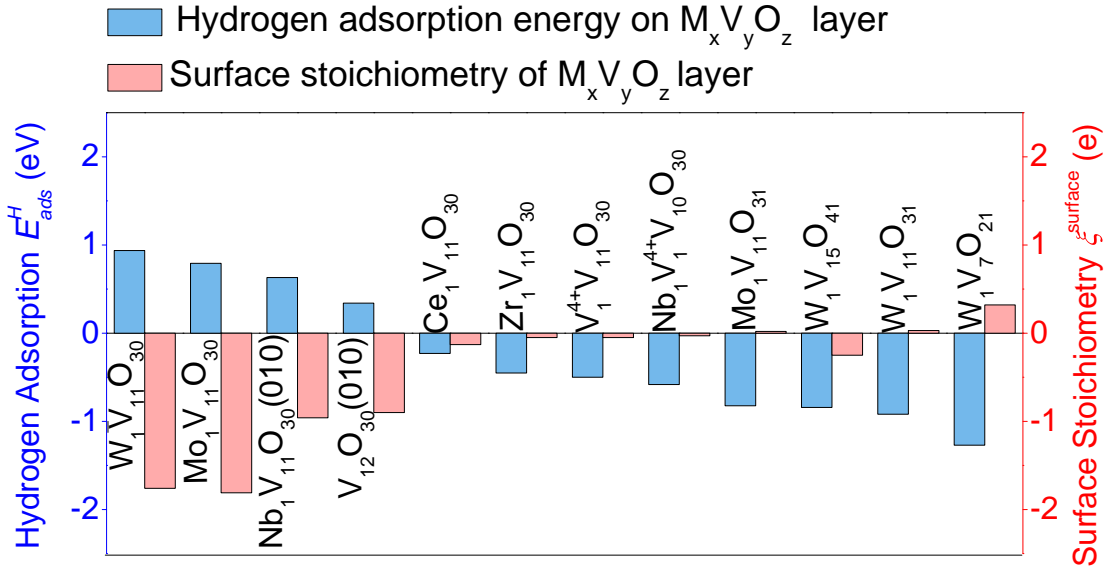
Figure 7: Hydrogen adsorption energy (blue bars) and surface stoichiometry (red bars) of various dopedv$M_xV_yO_z$ layers (M= W, Mo, Zr, Ce, V and Nb) with the dopant at the B site, as illustrated in Fig. 2.

the surface stoichiometry ξ^{surface} leads to a stronger hydrogen binding. Generally, there is a linear anti-correlation between ξ^{surface} and hydrogen adsorption energy on the considered doped vanadia catalysts.

Note that the choice of the dopant can influence both the efficiency of the catalyst recovery and the catalyst activation. Oxygen-excess configurations exhibit higher activities than oxygen-deficient configurations for NH_3 dissociation, NO adsorption, and also for the decomposition of the NH_xNO intermediates leading to N_2 formation. Among the oxygen-excess configurations, the Ce-doped vanadia is associated with a lower hydrogen adsorption energy than the W- and Mo-doped catalysts and with a lower reaction energy for NH_3 dissociation than the Nb- and Zr-doped catalysts. Thus Ce doping corresponds to a favorable compromise with respect to both catalyst activation and recovery. W- and Mo-doped oxygen-excess vanadia layers also allow facile NO adsorption. However, it will be hard to remove H species from them after N_2 formation.
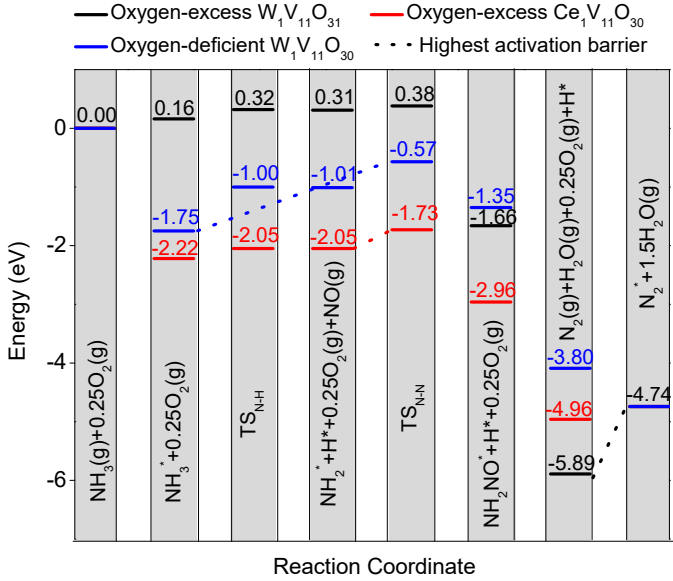
Reaction scheme and energy profile

Figure 8: Energy profile of the SCR reaction on oxygen-excess $W_1V_{11}O_{31}$, $Ce_1V_{11}O_{30}$, and oxygen-deficient $W_1V_{11}O_{30}$.

In this section, we discuss the whole SCR pathway using three exemplary doped vanadia catalysts, namely $W_1V_{11}O_{31}$, $W_1V_{11}O_{30}$, and $Ce_1V_{11}O_{30}$, addressing both catalyst activity and recovery. The energy profiles of the SCR reaction on these catalysts are plotted in Fig. 8. On the oxygen-excess W-doped vanadia catalyst ($W_1V_{11}O_{31}$, black line in Fig. 8), the NH_3 adsorption energy is slightly positive due to the high energetic cost of the catalyst deformation associated with NH_3 adsorption, which still limits the activity at high temperatures. However, NH_2 formation is hindered by a rather low barrier. Thus, the catalyst can capture NO and produce N_2 under suitable conditions. However, the high energy cost to remove the remaining adsorbed H species hinders catalyst recovery and leads to limited SCR activity at low temperatures. As a result, the operational temperature window is limited due to the small NH_3 adsorption energy gain and the high energy cost of H removal.

On the oxygen-deficient W-doped vanadia catalyst ($W_1V_{11}O_{30}$, blue line in Fig. 8), NH_3 adsorption is associated with a large energy gain. However, the activation of N-N formation requires a high energy cost of 1.22 eV (see the energy change from $NH_3^*+0.25O_2(g)$ to TS_{N-N},

25

highlighted by the blue-dashed line in Fig. 8). Consequently, this catalyst will only be active at rather high temperatures, although the reaction steps after NH_2NO formation towards the formation of N_2 and the catalyst recovery process are exothermic. Generally, the oxygen-excess W-doped vanadia catalysts are energetically more favorable than the oxygen-deficient configurations, and the improved catalytic performance upon increasing the oxygen content, as reflected by the higher surface stoichiometry $\xi^{surface}$, agrees with experimental findings.[25]

The oxygen-excess Ce-doped vanadia catalyst ($Ce_1V_{11}O_{30}$, red line in Fig. 8) exhibits the best SCR performance among the considered catalysts. There is a large adsorption energy gain upon ammonia adsorption of 2.22 eV, a low activation energies for N-N formation, and facile catalyst recovery. At the same time, the surface energy of NH_3-covered Ce-doped vanadia is 93.50 meV/$Å^2$, that is only slightly higher than the 91.39 meV/$Å^2$ for NH_3-covered W-doped vanadia, which indicates that Ce doping should lead to rather stable surface structures. Hence, Ce is expected to be a promising dopant for SCR vanadia catalysts. Our computational results are in line with the findings of experimental studies that reported an enhanced SCR activity for either Ce-doing[23] or mixed W- and Ce-doping[22,82] of the vanadia layer.

Finally we briefly address the so far disregarded reaction path through the ammonia adsorption at the Brønsted acid site (V-OH). Since NH_3 dissociation requires the presence of neighboring dangling oxygen bonds to capture the detached H atom, the vanadia configurations with densely packed dangling oxygen bonds, e.g., $M_3V_9O_{32}$ in Fig. 2d, require a high W or Mo concentration to maintain sufficient surface stability. However, according to our calculations, on such a surface, ammonia interacts with two neighboring dangling oxygen bonds and forms a hydrogen bond with one of them. As a result, NH_4^+ is created, which practically blocks the catalyst activation. For example, the reaction energy of NH_2NO formation from NH_4^+ is −0.13 eV and −0.02 eV on oxygen-excess $W_3V_9O_{32}$ and $W_3V_9O_{31}$, respectively. The energy gain is negligible compared to the energy gain upon NH_2NO formation from NH_2 of −2.25 and −1.09 eV at the Lewis acid site. Thus, the catalyst activation at the Brønsted

acid site is thermodynamically less favorable than at the Lewis acid site, which agrees well with the experimental findings.[10]

Conclusions

We have performed first-principles electronic structure calculations in order to provide a basic understanding of the selective catalytic reduction of nitric oxide by ammonia on doped titania-supported vanadia catalysts. We have studied the influence of dopants on all crucial reaction steps, the catalyst activation by NH_3 adsorption and NH_2 formation, N-N coupling by NO capturing, and the catalyst recovery by removing hydrogen. The presence of active dangling oxygen bonds turns out to be critical for the catalytic activity. According to our calculations the properties and distribution of dangling oxygen bonds can be controlled by the choice and the concentration of the dopants. In order to characterize the influence of the dopants on the catalytic activity, we have introduced a generalized surface stoichiometry that takes the nominal oxidation states of the atoms within the catalyst layer, polarization effects due to charge transfer between support and catalyst, local charge rearrangements, and the charge exchange with the reaction intermediates into account. We have demonstrated that the surface stoichiometry can act as a descriptor for the SCR activity, thus allowing the facile identification of suitable dopants to improve the performance of SCR catalysts, both with respect to their activity and their stability. Based on these considerations, we propose Ce doping of vanadia as a promising route towards more effective SCR catalysts. Furthermore, we expect that this descriptor will also be instrumental in identifying non-metallic catalysts with improved properties for other important catalytic reactions.

Acknowledgement

Data availability

The optimized geometric structures derived from electronic structure calculations that support the findings of this study are made available under the Creative Commons Attribution license (CC BY 4.0) on the NOMAD repository (https://nomad-lab.eu) under the following link: https://doi.org/10.17172/NOMAD/2024.11.03-1 .

References

(1) Idriss, H.; Seebauer, E. Reactions of ethanol over metal oxides. *J. Mol. Catal. A Chem.* **2000**, *152*, 201–212.

(2) Briand, L. E.; Farneth, W. E.; Wachs, I. E. Quantitative determination of the number of active surface sites and the turnover frequencies for methanol oxidation over metal oxide catalysts: I. Fundamentals of the methanol chemisorption technique and application to monolayer supported molybdenum oxide catalysts. *Catal. Today* **2000**, *62*, 219–229.

(3) Keller, F.; Döhn, J.; Groß, A.; Busch, M. Exploring the Mechanism of the Electrochemical Polymerization of CO_2 to Hard Carbon over CeO_2(110). *J. Phys. Chem. C* **2024**, *128*, 6280–6293.

(4) Prashanth, P.; Speth, R. L.; Eastham, S. D.; Sabnis, J. S.; Barrett, S. R. H. Post-combustion emissions control in aero-gas turbine engines. *Energy Environ. Sci.* **2021**, *14*, 916–930.

(5) Roy, S.; Hegde, M.; Madras, G. Catalysis for NO_x Abatement. *Appl. Energy* **2009**, *86*, 2283–2297.

(6) Consentino, L.; Pantaleo, G.; Parola, V. L.; Migliore, C.; Greca, E. L.; Liotta, L. F. NH$_3$-NO SCR Catalysts for Engine Exhaust Gases Abatement: Replacement of Toxic V$_2$O$_5$ with MnO$_x$ to Improve the Environmental Sustainability. *Top. Catal.* **2023**, *66*, 850–859.

(7) Xie, S.; Tan, W.; Li, Y.; Ma, L.; Ehrlich, S. N.; Deng, J.; Xu, P.; Gao, F.; Dong, L.; Liu, F. Copper Single Atom-Triggered Niobia–Ceria Catalyst for Efficient Low-Temperature Reduction of Nitrogen Oxides. *ACS Catal.* **2022**, *12*, 2441–2453.

(8) Li, M.; Sakong, S.; Groß, A. In Search of the Active Sites for the Selective Catalytic Reduction on Tungsten-Doped Vanadia Monolayer Catalysts Supported by TiO$_2$. *ACS Catal.* **2021**, *11*, 7411–7421.

(9) Zhu, M.; Lai, J.-K.; Tumuluri, U.; Wu, Z.; Wachs, I. E. Nature of Active Sites and Surface Intermediates during SCR of NO with NH$_3$ by Supported V$_2$O$_5$–WO$_3$/TiO$_2$ Catalysts. *J. Am. Chem. Soc.* **2017**, *139*, 15624–15627.

(10) Marberger, A.; Ferri, D.; Elsener, M.; Kröcher, O. The Significance of Lewis Acid Sites for the Selective Catalytic Reduction of Nitric Oxide on Vanadium-Based Catalysts. *Angew. Chem. Int. Ed.* **2016**, *55*, 11989–11994.

(11) Liu, Z.; Li, J.; Woo, S. I. Recent advances in the selective catalytic reduction of NOx by hydrogen in the presence of oxygen. *Energy Environ. Sci.* **2012**, *5*, 8799–8814.

(12) McFarland, E. W.; Metiu, H. Catalysis by Doped Oxides. *Chem. Rev.* **2013**, *113*, 4391–4427.

(13) Dong, C.; Yao, J.; Shi, J.; Han, L.; Qin, H.; Zhang, Z.; Zhang, Q.; Wang, J. Resource utilization strategy based on the deactivation mechanism of V$_2$O$_5$-WO$_3$/TiO$_2$ catalyst. *Fuel* **2025**, *381*, 133311.

(14) Xu, D.; Qu, W.; Liu, J.; Chen, J.; Fang, X.; Chen, L.; Ma, Z.; Liu, X.; Tang, X.; Chen, Y. Active sites of NO selective catalytic reduction over V_2O_5–WO_3/TiO_2. *J. Mater. Chem. A* **2023**, *11*, 24644–24650.

(15) Koebel, M.; Elsener, M.; Kleemann, M. Urea-SCR: a Promising Technique to Reduce NO_x Emissions from Automotive Diesel Engines. *Catal. Today* **2000**, *59*, 335–345.

(16) Busca, G.; Lietti, L.; Ramis, G.; Berti, F. Chemical and Mechanistic Aspects of the Selective Catalytic Reduction of NO_x by Ammonia over Oxide Catalysts: A Review. *Appl. Catal. B* **1998**, *18*, 1–36.

(17) Peng, Y.; Li, K.; Li, J. Identification of the active sites on CeO_2–WO_3 catalysts for SCR of NO_x with NH_3: An in situ IR and Raman spectroscopy study. *Appl. Catal. B* **2013**, *140-141*, 483–492.

(18) Cristallo, G.; Roncari, E.; Rinaldo, A.; Trifirò, F. Study of anatase–rutile transition phase in monolithic catalyst V_2O_5/TiO_2 and V_2O_5–WO_3/TiO_2. *Appl. Catal. A* **2001**, *209*, 249–256.

(19) Chen, W.; Zou, R.; Wang, X. Toward an Atomic-Level Understanding of the Catalytic Mechanism of Selective Catalytic Reduction of NO_x with NH_3. *ACS Catal.* **2022**, *12*, 14347–14375.

(20) Chen, G.; Chen, J.; Chen, X.; Yin, R.; Li, K.; Li, J. Monolith or Powder: Improper Sample Pretreatment May Mislead the Understanding of Industrial V_2O_5–WO_3/TiO_2 Catalysts Operated in Stationary Resources. *Environ. Sci. Technol.* **2022**, *56*, 16394–16399.

(21) Xu, G.; Li, H.; Yu, Y.; He, H. Dynamic Change of Active Sites of Supported Vanadia Catalysts for Selective Catalytic Reduction of Nitrogen Oxides. *Environ. Sci. Technol.* **2022**, *56*, 3710–3718.

(22) Chen, L.; Li, J.; Ge, M. Promotional Effect of Ce-doped V_2O_5-WO_3/TiO_2 with Low Vanadium Loadings for Selective Catalytic Reduction of NO_x by NH_3. *J. Phys. Chem. C* **2009**, *113*, 21177–21184.

(23) Liu, Z.; Zhang, S.; Li, J.; Zhu, J.; Ma, L. Novel V_2O_5–CeO_2/TiO_2 catalyst with low vanadium loading for the selective catalytic reduction of NO_x by NH_3. *Appl. Catal. B: Environ* **2014**, *158-159*, 11–19.

(24) Zhao, X.; Huang, L.; Li, H.; Hu, H.; Hu, X.; Shi, L.; Zhang, D. Promotional effects of zirconium doped $CeVO_4$ for the low-temperature selective catalytic reduction of NO_x with NH_3. *Appl. Catal. B* **2016**, *183*, 269–281.

(25) Zhu, L.; Zhong, Z.; Yang, H.; Wang, C. Effect of MoO_3 on vanadium based catalysts for the selective catalytic reduction of NO_x with NH_3 at low temperature. *Res. J. Environ. Sci.* **2017**, *56*, 169–179.

(26) Lian, Z.; Liu, F.; Shan, W.; He, H. Improvement of Nb Doping on SO_2 Resistance of VO_x/CeO_2 Catalyst for the Selective Catalytic Reduction of NO_x with NH_3. *J. Phys. Chem. C* **2017**, *121*, 7803–7809.

(27) Zhu, L.; Zhong, Z.; Xue, J.; Xu, Y.; Wang, C.; Wang, L. NH_3-SCR performance and the resistance to SO_2 for Nb doped vanadium based catalyst at low temperatures. *Res. J. Environ. Sci.* **2018**, *65*, 306–316.

(28) Świrk, K.; Delahay, G.; Zaki, A.; Adil, K.; Cadiau, A. Facile modifications of HKUST-1 by V, Nb and Mn for low-temperature selective catalytic reduction of nitrogen oxides by NH_3. *Catal. Today* **2022**, *384-386*, 25–32, 11th International Conference on Environmental Catalysis.

(29) Wachs, I. E. Progress in catalysis by mixed oxides: From confusion to catalysis science. *Catal. Today* **2022**,

(30) Gao, X.; Du, X.; Jiang, Y.; Zhang, Y.; Luo, Z.; Cen, K. A DFT study on the behavior of NO_2 in the selective catalytic reduction of nitric oxides with ammonia on a V_2O_5 catalyst surface. *J. Mol. Catal.* **2010**, *317*, 46–53.

(31) Arnarson, L.; Falsig, H.; Rasmussen, S. B.; Lauritsen, J. V.; Moses, P. G. A complete reaction mechanism for standard and fast selective catalytic reduction of nitrogen oxides on low coverage $VO_x/TiO_2(001)$ catalysts. *J. Catal.* **2017**, *346*, 188–197.

(32) Yin, X.; Han, H.; Miyamoto, A. Active site and mechanism of the selective catalytic reduction of NO by NH_3 over V_2O_5: A periodic first-principles study. *Phys. Chem. Chem. Phys.* **2000**, *2*, 4243–4248.

(33) Mason, M. M.; Lee, Z. R.; Vasiliu, M.; Wachs, I. E.; Dixon, D. A. Initial Steps in the Selective Catalytic Reduction of NO with NH_3 by TiO_2-Supported Vanadium Oxides. *ACS Catal.* **2020**, *10*, 13918–13931.

(34) Anstrom, M.; Topsøe, N.-Y.; Dumesic, J. Density functional theory studies of mechanistic aspects of the SCR reaction on vanadium oxide catalysts. *J. Catal.* **2003**, *213*, 115–125.

(35) Song, I.; Lee, J.; Lee, G.; Han, J. W.; Kim, D. H. Chemisorption of NH_3 on Monomeric Vanadium Oxide Supported on Anatase TiO_2: A Combined DRIFT and DFT Study. *J. Phys. Chem. C* **2018**, *122*, 16674–16682.

(36) Gilardoni, F.; Weber, J.; Baiker, A. Density functional investigation of the mechanism of the selective catalytic reduction of NO by NH_3 over vanadium oxide model clusters. *Int. J. Quantum Chem.* **1997**, *61*, 683–688.

(37) Yao, H.; Chen, Y.; Zhao, Z.; Wei, Y.; Liu, Z.; Zhai, D.; Liu, B.; Xu, C. Periodic DFT study on mechanism of selective catalytic reduction of NO via NH_3 and O_2 over the V_2O_5 (001) surface: Competitive sites and pathways. *J. Catal.* **2013**, *305*, 67–75.

(38) Gilardoni, F.; Weber, J.; Baiker, A. Mechanism of the Vanadium Oxide-Catalyzed Selective Reduction of NO by NH_3. A Quantum Chemical Modeling. *J. Phys. Chem. A* **1997**, *101*, 6069–6076.

(39) Suarez Negreira, A.; Wilcox, J. Role of WO_3 in the Hg Oxidation across the V_2O_5–WO_3–TiO_2 SCR Catalyst: A DFT Study. *J. Phys. Chem. C* **2013**, *117*, 24397–24406.

(40) Ali, Z.; Wu, Y.; Wu, Y.; Arain, Z.; Xu, M.; Lu, Q.; Ma, H.; Zhao, H. Inhibition effects of Pb species on the V_2O_5-MoO_3/TiO_2 catalyst for selective catalytic reduction of NO_x with NH_3: A DFT supported experimental study. *Appl. Surf. Sci.* **2020**, *525*, 146582.

(41) Wu, Y.; Ali, Z.; Lu, Q.; Liu, J.; Xu, M.; Zhao, L.; Yang, Y. Effect of WO_3 doping on the mechanism of mercury oxidation by HCl over V_2O_5/TiO_2 (001) surface: Periodic density functional theory study. *Appl. Surf. Sci.* **2019**, *487*, 369–378.

(42) Carbogno, C.; Behler, J.; Reuter, K.; Groß, A. Signatures of nonadiabatic O_2 dissociation at Al(111): First-principles fewest-switches study. *Phys. Rev. B* **2010**, *81*, 035410.

(43) Henß, A.-K.; Sakong, S.; Messer, P. K.; Wiechers, J.; Schuster, R.; Lamb, D. C.; Groß, A.; Wintterlin, J. Density fluctuations as door-opener for diffusion on crowded surfaces. *Science* **2019**, *363*, 715–718.

(44) Reuter, K.; Scheffler, M. Composition, structure, and stability of RuO_2(110) as a function of oxygen pressure. *Phys. Rev. B* **2001**, *65*, 035406.

(45) Rogal, J.; Reuter, K.; Scheffler, M. CO oxidation at Pd(100): A first-principles constrained thermodynamics study. *Phys. Rev. B* **2007**, *75*, 205433.

(46) Gossenberger, F.; Juarez, F.; Groß, A. Sulfate, Bisulfate, and Hydrogen Co-adsorption on Pt(111) and Au(111) in an Electrochemical Environment. *Front. Chem.* **2020**, *8*, 634.

(47) Groß, A. Grand-canonical Approaches to Understand Structures and Processes at Electrochemical Interfaces from an Atomistic Perspective. *Curr. Opin. Electrochem.* **2021**, *27*, 100684.

(48) Euchner, H.; Groß, A. Atomistic modeling of Li- and post-Li-ion batteries. *Phys. Rev. Mater.* **2022**, *6*, 040302.

(49) Kresse, G.; Furthmüller, J. Efficiency of Ab-Initio Total Energy Calculations for Metals and Semiconductors Using a Plane-Wave Basis Set. *Comp. Mater. Sci.* **1996**, *6*, 15–50.

(50) Kresse, G.; Furthmüller, J. Efficient Iterative Schemes for Ab Initio Total-Energy Calculations Using a Plane-Wave Basis Set. *Phys. Rev. B* **1996**, *54*, 11169–11186.

(51) Kresse, G.; Hafner, J. Ab Initio Molecular-Dynamics Simulation of the Liquid-Metal–Amorphous-Semiconductor Transition in Germanium. *Phys. Rev. B* **1994**, *49*, 14251–14269.

(52) Blöchl, P. E. Projector Augmented-Wave Method. *Phys. Rev. B* **1994**, *50*, 17953–17979.

(53) Kresse, G.; Joubert, D. From Ultrasoft Pseudopotentials to the Projector Augmented-Wave Method. *Phys. Rev. B* **1999**, *59*, 1758–1775.

(54) Perdew, J. P.; Burke, K.; Ernzerhof, M. Generalized Gradient Approximation Made Simple. *Phys. Rev. Lett.* **1996**, *77*, 3865–3868.

(55) Grimme, S.; Ehrlich, S.; Goerigk, L. Effect of the Damping Function in Dispersion Corrected Density Functional Theory. *J. Comput. Chem.* **2011**, *32*, 1456–1465.

(56) Dudarev, S. L.; Botton, G. A.; Savrasov, S. Y.; Humphreys, C. J.; Sutton, A. P. Electron-Energy-Loss Spectra and the Structural Stability of Nickel Oxide: An LSDA+U Study. *Phys. Rev. B* **1998**, *57*, 1505–1509.

(57) Wang, L.; Maxisch, T.; Ceder, G. Oxidation Energies of Transition Metal Oxides within the GGA + U Framework. *Phys. Rev. B* **2006**, *73*, 195107.

(58) Peng, Y.; Li, J.; Si, W.; Luo, J.; Wang, Y.; Fu, J.; Li, X.; Crittenden, J.; Hao, J. Deactivation and Regeneration of a Commercial SCR catalyst: Comparison with Alkali Metals and Arsenic. *Appl. Catal. B* **2015**, *168-169*, 195–202.

(59) Kristoffersen, H. H.; Metiu, H. Reconstruction of Low-Index α-V_2O_5 Surfaces. *J. Phys. Chem. C* **2015**, *119*, 10500–10506.

(60) Zhang, L.; Wen, B.; Zhu, Y.-N.; Chai, Z.; Chen, X.; Chen, M. First-principles calculations of water adsorption on perfect and defect WO_3(001). *Comput. Mater. Sci.* **2018**, *150*, 484–490.

(61) Koçer, C. P.; Griffith, K. J.; Grey, C. P.; Morris, A. J. First-principles study of localized and delocalized electronic states in crystallographic shear phases of niobium oxide. *Phys. Rev. B* **2019**, *99*, 075151.

(62) Chen, S.; Abdel-Mageed, A. M.; Li, M.; Cisneros, S.; Bansmann, J.; Rabeah, J.; Brückner, A.; Groß, A.; Behm, R. J. Electronic metal-support interactions and their promotional effect on CO_2 methanation on Ru/ZrO_2 catalysts. *J. Catal.* **2021**, *400*, 407–420.

(63) Tolba, S. A.; Allam, N. K. Computational Design of Novel Hydrogen-Doped, Oxygen-Deficient Monoclinic Zirconia with Excellent Optical Absorption and Electronic Properties. *Sci. Rep.* **2019**, *9*, 10159.

(64) Lei, Y.-H.; Chen, Z.-X. DFT+U Study of Properties of MoO_3 and Hydrogen Adsorption on MoO_3(010). *J. Phys. Chem. C* **2012**, *116*, 25757–25764.

(65) Li, M.-R.; Song, Y.-Y.; Wang, G.-C. The Mechanism of Steam-Ethanol Reforming on Co_{13}/CeO_{2-x}: A DFT Study. *ACS Catal.* **2019**, *9*, 2355–2367.

(66) Chen, H.-L.; Chen, H.-T. Role of hydroxyl groups for the O_2 adsorption on CeO_2 surface: A DFT+U study. *Chem. Phys. Lett.* **2010**, *493*, 269–272.

(67) Lazzeri, M.; Selloni, A. Stress-Driven Reconstruction of an Oxide Surface: The Anatase $TiO_2(001)$-(1×4)Surface. *Phys. Rev. Lett.* **2001**, *87*, 266105.

(68) Monkhorst, H. J.; Pack, J. D. Special Points for Brillouin-Zone Integrations. *Phys. Rev. B* **1976**, *13*, 5188.

(69) Kleemann, M.; Elsener, M.; Koebel, M.; Wokaun, A. Investigation of the Ammonia Adsorption on Monolithic SCR Catalysts by Transient Response Analysis. *Appl. Catal. B* **2000**, *27*, 231–242.

(70) NIST-JANAF Thermochemical Tables.

(71) Sheppard, D.; Terrell, R.; Henkelman, G. Optimization methods for finding minimum energy paths. *J. Chem. Phys.* **2008**, *128*, 134106.

(72) Limas, N. G.; Manz, T. A. Introducing DDEC6 Atomic Population Analysis: Part 2. Computed Results for a Wide Range of Periodic and Nonperiodic Materials. *RSC Adv.* **2016**, *6*, 45727–45747.

(73) Manz, T. A.; Limas, N. G. Introducing DDEC6 Atomic Population Analysis: Part 1. Charge Partitioning Theory and Methodology. *RSC Adv.* **2016**, *6*, 47771–47801.

(74) Kompio, P. G.; Brückner, A.; Hipler, F.; Auer, G.; Löffler, E.; Grünert, W. A New View on the Relations between Tungsten and Vanadium in V_2O_5-WO_3/TiO_2 Catalysts for the Selective Reduction of NO with NH_3. *J. Catal.* **2012**, *286*, 237–247.

(75) Kong, M.; Liu, Q.; Jiang, L.; Tong, W.; Yang, J.; Ren, S.; Li, J.; Tian, Y. K^+ Deactivation of V_2O_5-WO_3/TiO_2 Catalyst during Selective Catalytic Reduction of NO with NH_3: Effect of Vanadium Content. *Chem. Eng. J.* **2019**, *370*, 518–526.

(76) Kompio, P. G.; Brückner, A.; Hipler, F.; Auer, G.; Löffler, E.; Grünert, W. A new view on the relations between tungsten and vanadium in V_2O_5-WO_3/TiO_2 catalysts for the selective reduction of NO with NH_3. *J. Catal.* **2012**, *286*, 237–247.

(77) Li, M.; Groß, A.; Behm, R. J. Effect of O-Vacancy Concentration and Proximity on Electronic Metal–Support Interactions: Ru/ZrO$_2$ Catalysts. *ACS Catalysis* **2022**, *12*, 10065–10079.

(78) Zabilska, A.; Clark, A. H.; Moskowitz, B. M.; Wachs, I. E.; Kakiuchi, Y.; Copéret, C.; Nachtegaal, M.; Kröcher, O.; Safonova, O. V. Redox Dynamics of Active VO$_x$ Sites Promoted by TiO$_x$ during Oxidative Dehydrogenation of Ethanol Detected by Operando Quick XAS. *JACS Au* **2022**, *2*, 762–776.

(79) Lietti, L.; Alemany, J.; Forzatti, P.; Busca, G.; Ramis, G.; Giamello, E.; Bregani, F. Reactivity of V$_2$O$_5$-WO$_3$/TiO$_2$ catalysts in the selective catalytic reduction of nitric oxide by ammonia. *Catal. Today* **1996**, *29*, 143–148, Second Japan-EC Joint Workshop on the Frontiers of Catalytic Science and Technology for Energy, Environment and Risk Prevention.

(80) Xu, Y.; Ruban, A. V.; Mavrikakis, M. Adsorption and Dissociation of O$_2$ on Pt-Co and Pt-Fe Alloys. *J. Am. Chem. Soc.* **2004**, *126*, 4717–4725.

(81) Sakong, S.; Mosch, C.; Lozano, A.; Busnengo, H. F.; Groß, A. Lowering Energy Barriers in Surface Reactions through Concerted Reaction Mechanisms. *ChemPhysChem* **2012**, *13*, 3467–3471.

(82) Chen, L.; Li, J.; Ge, M. DRIFT Study on Cerium-Tungsten/Titiania Catalyst for Selective Catalytic Reduction of NO$_x$ with NH$_3$. *Environ. Sci. Technol.* **2010**, *44*, 9590–9596.